Smart Mater. Struct. **20** (2011) 015025 (12pp) doi:10.1088/0964-1726/20/1/015025

Modelling and simulation of wirelessly and securely interrogated low-powered actuators for bio-MEMS

Don W Dissanayake[1,2], **Said Al-Sarawi**[1,2,3] **and Derek Abbott**[1,2,3]

[1] Centre for High Performance Integrated Technologies and Systems (CHiPTec), University of Adelaide, SA 5005, Australia
[2] School of Electrical and Electronic Engineering, University of Adelaide, SA 5005, Australia
[3] Centre for Biomedical Engineering (CBME), University of Adelaide, SA 5005, Australia

E-mail: don@eleceng.adelaide.edu.au

Received 14 June 2010, in final form 1 November 2010
Published 23 December 2010
Online at stacks.iop.org/SMS/20/015025

Abstract
This paper presents modelling and analysis of microactuators that are designed for implantable bio-MEMS applications. Microactuators are considered to be a major component of microvalves and micropumps. A novel interrogation methodology is implemented, which is based on surface acoustic wave (SAW) devices and wireless transcutaneous RF communication. This unique combination of technologies results in a novel microactuator that can be remotely and securely interrogated by an RF system, with the advantage of no power requirements at the actuator site. ANSYS based finite element analysis (FEA) is performed to model the microactuator, and a Rayleigh–Ritz method based analytical model is developed to investigate the validity of FEA results. During FEA, a 3D model of the microactuator is developed, and a coupled-field analysis is carried out to model the electrostatic–solid interaction between the microactuator and the SAW device. Consequently, detailed 3D modelling and transient results are presented, and the low-powered microdisplacements at low frequencies are clearly demonstrated.

(Some figures in this article are in colour only in the electronic version)

1. Introduction

Due to the rapid growth in micro-electromechanical systems (MEMS) technology, design, development, and realization of miniature devices for biomedical implants have become a reality. In particular, bio-MEMS based implantable total drug delivery systems have shown the potential to offer new paradigms in biomedicine and biology. Bio-MEMS based micro-drug-delivery systems consist of various types of MEMS devices such as microactuators, micropumps, microsensors, microvalves, microneedles, microfluidic channels, and drug reservoirs.

Generally, microactuators take a critical role in commonly used mechanical micropumps that form a fundamental and a critical part of a drug delivery system. Such actuation sources facilitate effective transfer of an accurate amount of fluid/drug to a targeted location. The design of a suitable actuator device to pump the fluid at the microscale, for accurate operation, is of great importance. Many types of microactuators have been developed to match different requirements for various applications [1, 2].

However, the lack of availability of accurate and easy to use, implantable and low-powered actuation mechanisms has been identified as a significant problem [3]. Furthermore, the ease of control of implantable biological devices would be greatly improved by incorporation of wireless and secure actuator systems with no battery attached to the device.

1.1. Wireless and secure interrogation

With the advancements in RF-MEMS and bio-MEMS technologies, there is an increasing interest in designing biotelemetry devices [4]. Currently, there are various implants in use and in development [5, 6]. Remotely interrogated implantable actuators and drug pumps have been developed for pain relief applications such as for chronic pain due to cancer,

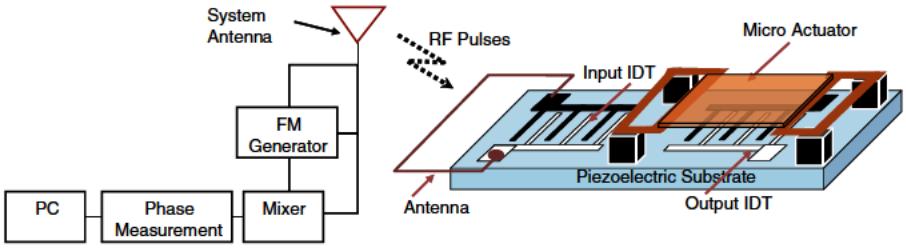

Figure 1. Wireless interrogation unit for SAW based actuator. The microactuator is placed on top of the output IDT of a SAW device. The SAW device consists of a piezoelectric substrate, input IDT, and output IDT. The input IDT is connected to a micro-antenna for wireless interrogation.

chronic back leg pain, painful neuropathy [5], and complex regional pain syndrome (CRPS). However, large size due to the in-built active electronics has been a major drawback in these devices.

The surface acoustic wave (SAW) devices are used to develop micromachines such as ultrasonic micromotors and fluid transfer methodologies such as flexural micropumps [7, 8]. Furthermore, the SAW technology for microactuations provides the great benefit of control and interrogation of devices remotely, without direct physical user intervention [2, 3, 9].

In this paper, SAW based novel batteryless and low-powered, secure, and wireless interrogation as well as actuation mechanisms for implantable MEMS devices are introduced and investigated. In section 2, the use of SAW devices for wireless communication is summarized and in section 3 the novel interrogation methodology is presented. Section 4 explains the operation of the SAW device based microactuator. The underlying theoretical model is then elaborated in section 5 and followed by section 6, which presents a method to derive the electric potential for electrostatic actuation. Section 7 shows a theoretical boundary condition analysis for the proposed model. Section 9 presents detailed finite element modelling (FEM) of the actuator. Then simulation results are discussed in section 10, followed by the conclusion in section 11.

2. SAW devices for wireless and secure interrogation

As shown in figure 1, a SAW device consists of a solid substrate with input and output inter-digital transducers (IDT). IDTs provide a coupling between the electrical signal received (or transmitted) and the mechanical stress waves generated on the piezoelectric substrate. Acoustic waves in these devices are propagating as surface waves, and hence can be perturbed easily by modifications to the substrate surface. Such features have enabled a large number of resonant sensors for applications such as chemical sensors [10], gyroscopes [2], and accelerometers [11]. SAW devices also find application in oscillators, pulse compressors, convolvers, correlators, multiplexers and demultiplexers [10]. In implantable bio-MEMS, it is important for the device to be securely operated, and not to be triggered by spurious RF signals. The present authors' previous research work [12] illustrated that a SAW correlator is an ideal choice to incorporate the secure interrogation of the device. SAW correlator is a special type of SAW device, consisting of a coded IDT to ensure that the device responds only to a matched RF signal [3, 13, 14].

It is worth noting that, as shown in figure 1, the energy received from the receiver antenna is transduced to the input IDT, and through the SAW correlator mechanism to the output IDT, since the critical signal comparison takes place at the output IDT. Hence, the SAW device performs a significant role in this novel interrogation methodology by facilitating a simple and passive mechanism for secure actuations.

3. Interrogation methodology

The proposed interrogation mechanism in this research is therefore a novel combination of two well established SAW based technologies; one is for RF communication and the other is for the incorporation of secure interrogation.

As presented in figure 1, for microactuations, a conductive plate (or actuator) is placed on top of the output IDT, with a separation of few micrometres, using an air gap. In the arrival of a matched code at the output IDT, a low-powered electrostatic actuation force is generated on the plate, causing micro-deformations in the conductive plate.

As can be seen from figure 2, to prevent high frequency vibrations (megahertz range) of the proposed microactuator, the trigger frequency of the interrogating signal (f_{RF}) is scaled down (hertz range), compared to the actual SAW frequency (f_{SAW}), such that $f_{RF} \ll f_{SAW}$.

4. Microactuator operating principle

Figure 3 depicts the structural design for the SAW based microactuator. The actuator is made of a conductive material, or alternatively it can be made of a material such as silicon (Si) or silicon nitride (Si_3N_4) and the bottom surface of the microactuator can be coated with a thin conductive material such as gold, platinum or aluminium. The SAW substrate is made out of 128-YX-lithium niobate ($LiNbO_3$), as it consists of a higher electromechanical coupling. The output IDT and the conductive plate are used to generate an air-gap coupled SAW based electrostatic actuator.

The device operation is as follows. The input IDT generates Rayleigh waves using the inverse piezoelectric effect based on the RF signal that is being fed to the SAW device through the microstrip antenna. If the embedded code in the SAW IDT is matched with the code embedded in the RF

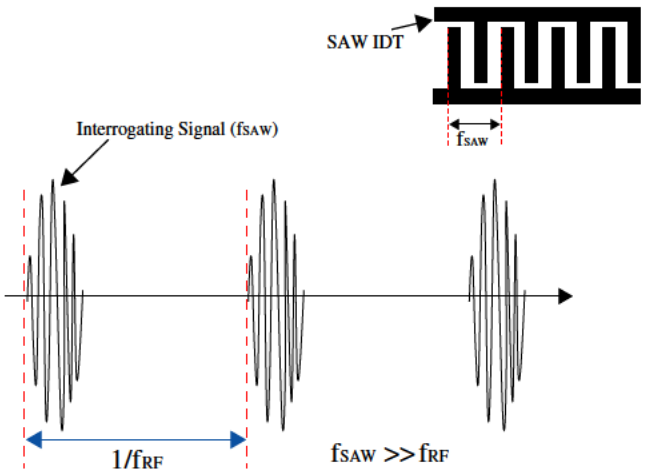

Figure 2. The relationship between the SAW frequency and the trigger frequency of the interrogating signal. The SAW frequency (f_{SAW}) is determined by the IDT finger pattern. The trigger frequency of the interrogating signal (f_{RF}) is a very much scaled down value, compared to f_{SAW}.

signal, the output IDT regenerates the electric signal using the piezoelectric effect of the SAW device. The generated electrostatic field between this propagating electric potential wave and the conductive plate creates a compulsive and repulsive force between the two. Since the conductive plate is a thin flexural plate, it bends as a function of the applied electrostatic field, enabling its use as a microactuator.

5. Theoretical model

The IDT patterns in a SAW device can be considered as a periodic structure. As presented in figure 3, the direction of periodicity is denoted by x_1, the surface normal direction by x_3, and their perpendicular direction by x_2, following a right-handed coordinate system. The dimensional extension of electrodes in the x_2 direction (length of the IDT fingers) is much larger in comparison to the periodicity. Additionally, a homogeneous material topology is assumed in the x_2 direction for this analysis.

5.1. Piezoelectric equations for the SAW substrate

In piezoelectric analysis, quasi-static electric field is achieved by setting the permeability to zero, corresponding to an infinite speed of the electromagnetic wave. Using Maxwell's equations, the electromagnetic quasi-static approximation can be written as

$$E_i = -\frac{\partial \Phi}{\partial x_i}, \tag{1}$$

$$\nabla \cdot D = 0, \tag{2}$$

where E is the electric field intensity, Φ is the electric potential, D is the electric flux density (dielectric displacement) and x_i (for $i = 1$–3) shows the direction of interest as shown in figure 3. Here, equation (2) elaborates the fact that piezoelectric materials are insulators, hence there are no free volume charges [15]. Moreover, from the mechanical

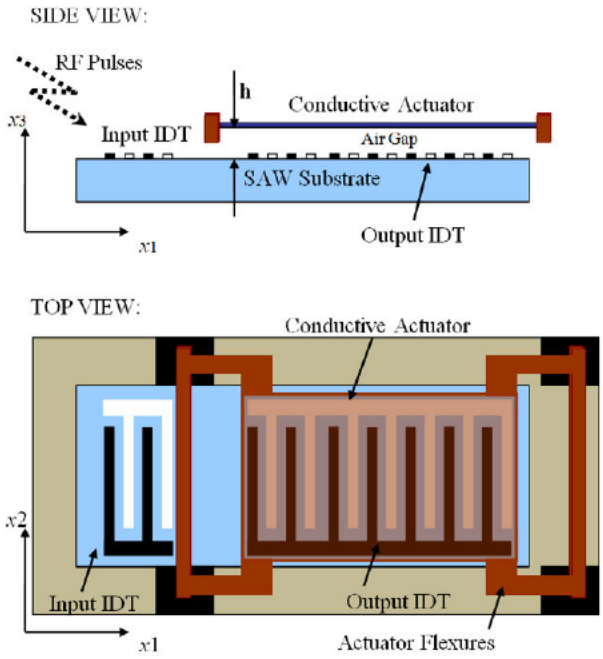

Figure 3. Concept drawing of the SAW actuator model. Side view: an air-gap separated conductive actuator is placed above the output IDT. Top view: the actuator consists of flexures to reduce the spring constant. h is the height of the air gap.

equations of motion, the relationship between the mechanical displacement u and the mechanical stress T is given by

$$\rho \frac{\partial^2 u_i}{\partial t^2} = \sum_j \frac{\partial T_{ij}}{\partial x_i}, \tag{3}$$

where ρ is the density of the piezoelectric substrate. For a piezoelectric medium, the relation between the mechanical strain S and mechanical displacement u can be written as

$$S_{ij} = \frac{1}{2}\left[\frac{\partial u_i}{\partial x_j} + \frac{\partial u_j}{\partial x_i}\right]. \tag{4}$$

To investigate the behaviour of the electric potential and the mechanical displacement of the SAW, the constitutive equations for piezoelectric material also need to be considered. The constitutive equations for piezoelectric material can be obtained by extending Hook's law and the electrostatic equation for the electric flux density. Therefore, the relationship between D, E, T and S in a SAW substrate can be written as

$$T_{ij} = \sum_k \sum_l c^E_{ijkl} S_{kl} - \sum_k e_{kij} E_k, \tag{5}$$

$$D_i = \sum_j \sum_k e_{ijk} S_{jk} + \sum_j \varepsilon^S_{ij} E_j, \tag{6}$$

where c_{ijkl} is the stiffness tensor for constant electric field, e_{ijk} is the piezoelectric coupling tensor (e_{kij} is the corresponding transpose tensor of e_{ijk}), ε_{ij} is the permittivity tensor for constant strain and i, j, k, l vary from 1 to 3. The above tensors are elements in the mechanical stiffness matrix [c],

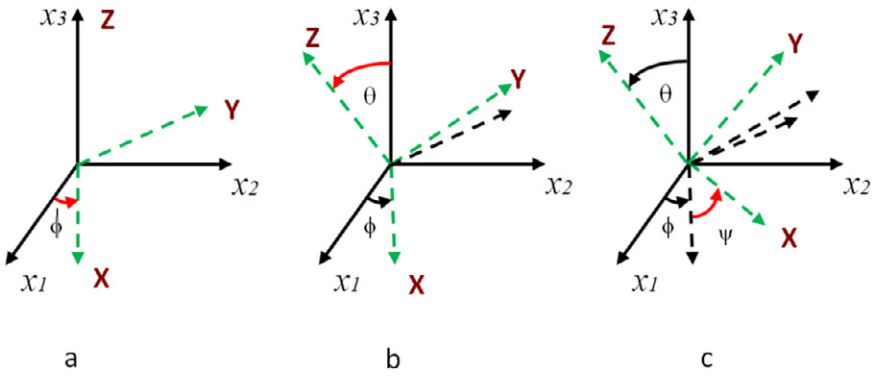

Figure 4. Transformation of coordinate system using the X-convention. $x_1x_2x_3$ is the structural coordinate system and XYZ is the crystal coordinate system. x_1 determines the wave propagation direction and x_3 is normal to the crystal surface. Initially both of these axes are parallel to each other. While the structural coordinate axes always remain same, the crystal axes XYZ are rotated by an angle ϕ around the Z axis, then by an angle θ around the X axis and finally by an angle ψ once again around the Z axis. The direction cosines are derived based on the Euler angles.

the piezoelectric matrix $[e]$, and the permittivity matrix $[\boldsymbol{\varepsilon}]$ respectively.

Equations (1)–(6) lead to a system of four coupled equations, which are represented by equations (7) and (8).

$$\sum_j \sum_k \left[e_{kij} \frac{\partial^2 \Phi}{\partial x_j \partial x_k} + \sum_l c^E_{ijkl} \frac{\partial^2 u_k}{\partial x_j \partial x_l} \right] = \rho \frac{\partial^2 u_i}{\partial t^2}, \tag{7}$$

$$\sum_i \sum_j \left[\varepsilon^S_{ij} \frac{\partial^2 \Phi}{\partial x_i \partial x_j} - \sum_k e_{ijk} \frac{\partial^2 u_j}{\partial x_i \partial x_k} \right] = 0. \tag{8}$$

The relationship between mechanical displacement and electric potential is considered in a semi-infinite, isotropic and homogeneous linear elastic space. The piezoelectric crystal cut ensures the Rayleigh wave propagates in the x_1–x_3 sagittal plane as shown in figure 3.

The method of partial waves is used to solve the wave propagation phenomenon for the SAW actuator model, as it is a commonly used technique to analyse different SAW modes on anisotropic substrates such as piezoelectrics [15–17]. The plane wave solutions of the form given in equations (9) and (10) are considered for the mathematical modelling of this device,

$$u^m_j(x_1, x_3, t) = \alpha^m_j \mathrm{e}^{\mathrm{i}kb^m x_3} \mathrm{e}^{\mathrm{i}k(x_1 - vt)}, \tag{9}$$

$$\Phi^m(x_1, x_3, t) = \alpha^m_4 \mathrm{e}^{\mathrm{i}kb^m x_3} \mathrm{e}^{\mathrm{i}k(x_1 - vt)}, \tag{10}$$

where the α^m_j values are linear coefficients that depend on the decaying constant b^m, v is the phase velocity of the wave, k $(=2\pi/\lambda)$ is the wavevector, λ is the wavelength, i is the standard imaginary unit $(=\sqrt{-1})$, $m = 1$–4 and $j = 1$–3.

Using equations (7)–(10), a linear system for the coefficients α^m_j can be obtained and solved. In solving these equations, however, it is necessary to transform the material parameters of the SAW substrate to match the coordinate system of the problem, as discussed below.

5.2. Transformation of coordinates

In the equations of motion the material parameters are expressed in terms of structural coordinate axes that are selected for convenient boundary condition and excitation requirements. However, the material parameters are presented in the form of $[c]$, $[\boldsymbol{\varepsilon}]$, and $[e]$ matrices as was mentioned in section 5.1, and these are expressed according to the crystalline axes. Therefore, it is necessary to transform the material parameters to match the coordinate system of the problem. Generally, the parameters are transformed using a transformation matrix $[\boldsymbol{r}]$

$$[\boldsymbol{r}] = \begin{bmatrix} \cos\psi\cos\phi & \cos\psi\sin\phi & \sin\psi\sin\theta \\ -\cos\theta\sin\phi\sin\psi & +\cos\theta\cos\phi\sin\psi & \\ \sin\psi\cos\theta & -\sin\psi\sin\phi & \cos\psi\sin\theta \\ -\cos\theta\sin\phi\cos\psi & +\cos\theta\cos\phi\cos\psi & \\ \sin\theta\sin\phi & -\sin\theta\cos\phi & \cos\theta \end{bmatrix} = \begin{bmatrix} r_{11} & r_{12} & r_{13} \\ r_{21} & r_{22} & r_{23} \\ r_{31} & r_{32} & r_{33} \end{bmatrix}.$$

Elements of this matrix are the direction cosines between the crystalline axis and the problem axis [11, 18, 19]. As depicted in figure 4, the X-convention is followed in this research for specifying the order of rotation of the axes.

Once the transformation matrix is defined, the matrices that define the crystal properties ($[c]$, $[\boldsymbol{\varepsilon}]$, and $[e]$) are transformed using the bond-transformation procedure [20]. The advantage associated with the this procedure, for stiffness and compliance, is that bond transformation is directly applied on stiffness or compliance constants given in abbreviated subscript notation. The transformation laws of this procedure can be shown as

$$[c_r] = [M_B][c][M_B^{\mathrm{T}}], \tag{11}$$

$$[e_r] = [M_B][e][r^{\mathrm{T}}], \tag{12}$$

$$[\boldsymbol{\varepsilon}_r] = [\boldsymbol{r}][\boldsymbol{\varepsilon}][\boldsymbol{r}^{\mathrm{T}}], \tag{13}$$

where

$$[M_B] = \begin{bmatrix} r_{11}^2 & r_{12}^2 & r_{13}^2 & 2r_{12}r_{13} & 2r_{11}r_{13} & 2r_{11}r_{12} \\ r_{21}^2 & r_{22}^2 & r_{23}^2 & 2r_{22}r_{23} & 2r_{21}r_{23} & 2r_{21}r_{22} \\ r_{31}^2 & r_{32}^2 & r_{33}^2 & 2r_{32}r_{33} & 2r_{31}r_{33} & 2r_{31}r_{32} \\ r_{21}r_{31} & r_{22}r_{32} & r_{23}r_{33} & r_{22}r_{33}+r_{32}r_{23} & r_{21}r_{33}+r_{31}r_{23} & r_{21}r_{32}+r_{31}r_{22} \\ r_{11}r_{31} & r_{12}r_{32} & r_{13}r_{33} & r_{12}r_{33}+r_{32}r_{13} & r_{31}r_{13}+r_{11}r_{33} & r_{11}r_{32}+r_{31}r_{12} \\ r_{11}r_{21} & r_{12}r_{22} & r_{13}r_{23} & r_{12}r_{23}+r_{22}r_{13} & r_{11}r_{23}+r_{21}r_{13} & r_{11}r_{22}+r_{21}r_{12} \end{bmatrix}.$$

is the bond-transformation matrix; $[r^{\mathrm{T}}]$ denotes the transpose of the matrix $[r]$. $[c_r]$ is the transformed stiffness matrix, $[e_r]$ is the transformed piezoelectric matrix, and $[\varepsilon_r]$ is the transformed permittivity matrix.

5.3. Calculations for a specific SAW substrate

In order to derive the specific plane wave equations for a selected crystal, partial wave equations (9) and (10) are substituted into equations (7) and (8) with the rotated material parameters. As a result, the following eigenvalue problem can be obtained.

$$\mathbf{M} \cdot \boldsymbol{\alpha} = 0. \tag{14}$$

Alternatively, the above equation can be written as

$$\begin{bmatrix} m_{11}-\rho v^2 & m_{12} & m_{13} & m_{14} \\ m_{12} & m_{22}-\rho v^2 & m_{23} & m_{24} \\ m_{13} & m_{23} & m_{33}-\rho v^2 & m_{34} \\ m_{14} & m_{24} & m_{34} & m_{44}-\rho v^2 \end{bmatrix} \times \begin{bmatrix} \alpha_1 \\ \alpha_2 \\ \alpha_3 \\ \alpha_4 \end{bmatrix} = 0. \tag{15}$$

The matrix coefficients in equation (15) are shown below.

$$m_{11} = c_{55}b^2 + 2c_{15}b + c_{11} \Rightarrow m_{11} = c_{55}b^2 + c_{11}$$
$$m_{12} = c_{45}b^2 + (c_{14}+c_{56})b + c_{16} \Rightarrow m_{12} = (c_{14}+c_{56})b$$
$$m_{13} = c_{35}b^2 + (c_{13}+c_{55})b + c_{15} \Rightarrow m_{13} = (c_{13}+c_{55})b$$
$$m_{14} = e_{53}b^2 + (e_{51}+e_{13})b + e_{11} \Rightarrow m_{14} = (e_{51}+e_{13})b$$
$$m_{22} = c_{44}b^2 + 2c_{46}b + c_{66} \Rightarrow m_{22} = c_{44}b^2 + c_{66}$$
$$m_{23} = c_{34}b^2 + (c_{36}+c_{45})b + c_{56} \Rightarrow m_{23} = c_{34}b^2 + c_{56}$$
$$m_{24} = e_{43}b^2 + (e_{41}+e_{63})b + e_{61} \Rightarrow m_{24} = e_{43}b^2 + e_{61}$$
$$m_{33} = c_{33}b^2 + 2c_{35}b + c_{55} \Rightarrow m_{33} = c_{33}b^2 + c_{55}$$
$$m_{34} = e_{33}b^2 + (e_{31}+e_{53})b + e_{51} \Rightarrow m_{34} = e_{33}b^2 + e_{51}$$
$$m_{44} = -(\varepsilon_{33}b^2 + 2\varepsilon_{13}b + \varepsilon_{11}) \Rightarrow m_{44} = -(\varepsilon_{33}b^2 + \varepsilon_{11}).$$

In order to evaluate the non-trivial solution for equation (15), the eigenvalue problem, $\det(\mathbf{M}) = 0$, is required to be solved. This results in a system of characteristic equations for displacement amplitudes and electric potential in which the phase velocity v of the wave is used as an unknown parameter. In the general case, this system of characteristic equations is reduced to an eighth order polynomial in the decaying constant b for a given value of phase velocity. However, the resulting roots of b are either purely real or complex conjugate pairs. Since these roots leads to Rayleigh waves that decay with the depth along x_3, only the roots with negative imaginary parts are accepted to be consistent with the physical meaning of wave propagation in piezoelectric media [21, 22]. There are four such roots for b (denoted as b^m for $m = 1$–4), and for each such value there exists a unique eigenvector $\boldsymbol{\alpha}^m$. A general solution is then obtained as a linear combination of partial waves such that each wave decays almost to zero as it shifts into the crystal depth at a distance of several wavelengths from the surface ($x_3 = 0$). The solution consists of three displacement components u_j ($j = 1$–3) and the electric potential Φ as described by equations (16) and (17).

$$u_j(x_1, x_3, t) = \left[\sum_m C_m \alpha_j^m \mathrm{e}^{\mathrm{i}kb^m x_3}\right] \mathrm{e}^{\mathrm{i}k(x_1 - vt)}, \tag{16}$$

$$\Phi(x_1, x_3, t) = \left[\sum_m C_m \alpha_4^m \mathrm{e}^{\mathrm{i}kb^m x_3}\right] \mathrm{e}^{\mathrm{i}k(x_1 - vt)}. \tag{17}$$

The weighting coefficients C_m of these plane waves are chosen to satisfy the mechanical and electrical boundary conditions at the surface of the piezoelectric substrate specific to this SAW based actuator model, which is discussed in detail in section 7, after deriving an expression for the electric potential at the output IDT using equation (17).

6. Electric potential at output IDT

In order to determine the electrostatic field generated between the output IDT and the conductive plate, the evaluation of the electric potential at the output IDT is required. Here, once the plane wave equation is evaluated for the electric potential wave in the SAW device (equation (17)), an analysis is carried out to evaluate an expression for the electric potential at the output IDT. In achieving this, the following assumptions and simplification are made to the design apart from previously mentioned simplifications.

(i) The crystal cut is best set for a SAW propagation in the x_1 direction to allow an orthogonal interaction between the SAW and the output IDT.
(ii) The IDT is oriented such that a SAW is generated in the direction of maximum SAW propagation speed.
(iii) The SAW is assumed to pass the output IDT once, and interact with no reflections caused by impedance mismatches [21, 22].
(iv) The SAW interacts with the IDT in the near field where the SAW can be treated as a travelling wave.

Due to the periodic nature of the propagating waves and the placement of the IDTs, the analysis is initially carried out only for a single period, and then extended to the whole structure. The single period placement of the output IDT is shown in figure 5.

As explained in figure 5, each finger in the IDT is assigned a negative or positive value that is determined by the finger's connection to either a positive or negative bus bar. Therefore, the output IDT fingers are represented as square waves with the period defining the wavelength of the SAW and the duty cycle defining the finger width [23]. This width is $\frac{\lambda}{4}$ for a metallization ratio of 0.5. For the SAW based electrostatic actuator model, initially a basic model of the IDT configuration is used.

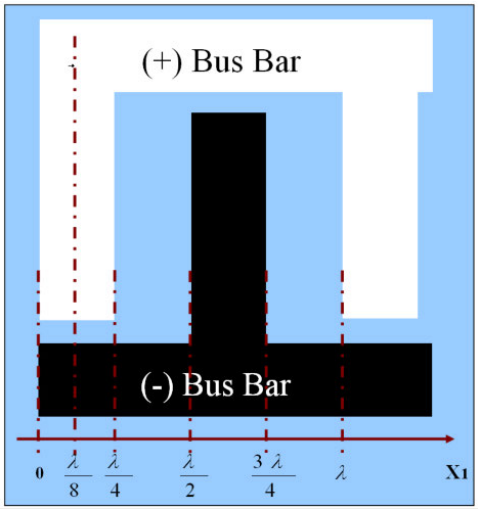

Figure 5. Periodic IDT finger representation for one wavelength (λ) with a metallization ratio of $\frac{1}{2}$.

While the output IDT is considered as a combination of square waves, the SAW is defined as a propagating plane wave as was elaborated in section 5.3. In order to obtain the time response of the SAW interaction with the output IDT, a cross-correlation is applied to the SAW and the IDT signals. Cross-correlation is a method by which two different functions are compared over time with one time-fixed function and one time-shifted function. Within one wavelength of the IDT, the analysis has to be carried out in two parts, considering the space above the output IDT fingers ($0 \leqslant x_1 \leqslant \frac{\lambda}{4} \cup \frac{\lambda}{2} \leqslant x_1 \leqslant \frac{3\lambda}{4}$) and the space above the output IDT gap between fingers ($\frac{\lambda}{4} < x_1 < \frac{\lambda}{2} \cup \frac{3\lambda}{4} < x_1 < \lambda$). This is because the metal based IDT fingers consist of an equipotential distribution for a given time, and the gaps between the fingers consist of a space varying electric potential distribution in the x_1 direction.

IDT segment in range ($0 \leqslant x_1 \leqslant \frac{\lambda}{4} \cup \frac{\lambda}{2} \leqslant x_1 \leqslant \frac{3\lambda}{4}$)

As shown in figure 6, analysis of a single IDT finger will serve as the basis for the analysis for a single periodic structure and then for the entire IDT structure. Therefore, the cross-correlation between the SAW potential signal $\Phi(x_1, x_3, t)$ and the first finger connected to the positive bus bar ($0 \leqslant x_1 \leqslant \frac{\lambda}{4}$) can be expressed as

$$\begin{aligned} C_+(x_1, x_3, t) &= (\Phi * g_{(+)})(x_1, x_3, t) \\ &= \int_0^{T/4} \Phi(x_1, x_3, t+\tau) \cdot g_{(+)}(\tau)\, \mathrm{d}\tau \\ &= \frac{\sqrt{2}}{kv} \Phi\left(x_1 - \frac{\lambda}{8}, x_3, t\right). \end{aligned} \tag{18}$$

Here, $g_{(+)}$ represents the positive square wave of the finger as can be seen from figure 6.

The electric potential at this IDT finger can be considered as the average value of the correlated signal $C_+(x_1, x_3, t)$ over the finger width f_w, due to the equipotential nature of the metal based fingers. As the metallization ratio is 0.5 in this analysis, $f_w = \lambda/4$ and this relates to $T/4$ in timescale, where T ($=\lambda/v$) is the time period of the SAW. Therefore, the electric potential

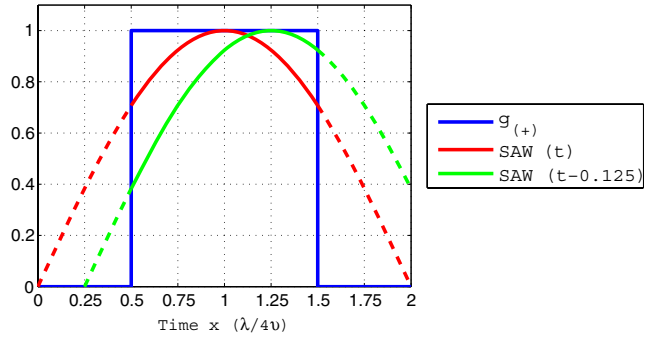

Figure 6. Superimposition of the SAW and a single finger of the output IDT. $g_{(+)}$ represents the equipotential behaviour of the conductive finger. Two SAWs are $T/8$ apart from one another.

generated at the first finger connected to the positive bus bar can be written as

$$\begin{aligned} V_+(x_1, x_3, t) &= \int_0^{\lambda/4} C_+(x_1, x_3, t)\, \mathrm{d}x_1 \\ &= \frac{2T}{\pi^2} \Phi\left(\frac{\lambda}{8}, x_3, t\right). \end{aligned} \tag{19}$$

By following an identical approach, the electric potential at the finger connected to the negative bus bar ($\frac{\lambda}{2} \leqslant x_1 \leqslant \frac{3\lambda}{4}$) can be derived and the result can be written as

$$V_-(x_1, x_3, t) = -\frac{2T}{\pi^2} \Phi\left(\frac{\lambda}{8}, x_3, t\right). \tag{20}$$

IDT segment in range ($\frac{\lambda}{4} < x_1 < \frac{\lambda}{2} \cup \frac{3\lambda}{4} < x_1 < \lambda$).

Once the analysis is simplified by considering the aforementioned assumptions and simplifications, the electric potential at the gaps between the fingers can be considered to consist of the same electric potential of the propagating SAW as shown in equation (17). Therefore

$$V_{\mathrm{gap}}(x_1, x_3, t) = \Phi(x_1, x_3, t). \tag{21}$$

Consequently, the total electric potential generated by a single period of the output IDT can be derived, and graphically elaborated in figure 7. Due to the periodic nature of the IDT, the periodic expression can be easily extended to derive the electric potential for the full output IDT. Therefore, for an output IDT with N_p finger pairs, the total electrostatic potential at the output IDT can be expressed as

$$\Phi(x_1, x_3, t) = \begin{cases} \Psi, & \text{for } n\lambda \leqslant x_1 \leqslant (\frac{1}{4}+n)\lambda \\ \Omega, & \text{for } (\frac{1}{4}+n)\lambda < x_1 < (\frac{1}{2}+n)\lambda \\ -\Psi, & \text{for } (\frac{1}{2}+n)\lambda \leqslant x_1 \leqslant (\frac{3}{4}+n)\lambda \\ -\Omega, & \text{for } (\frac{3}{4}+n)\lambda < x_1 < (1+n)\lambda \end{cases} \tag{22}$$

where $\Psi = V_+(x_1, x_3, t) = \frac{2T}{\pi^2}\Phi(\frac{\lambda}{8}, x_3, t)$, $\Omega = V_{\mathrm{gap}}(x_1, x_3, t) = \Phi(x_1, x_3, t)$, and $n = 0, 1, 2, \ldots, (N_p - 1)$.

A boundary condition analysis is then carried out to specify values for the weighting coefficients in equation (22).

7. Boundary condition analysis

The weighting coefficients in equations (16) and (17) need to be determined based on the electrical and mechanical boundary

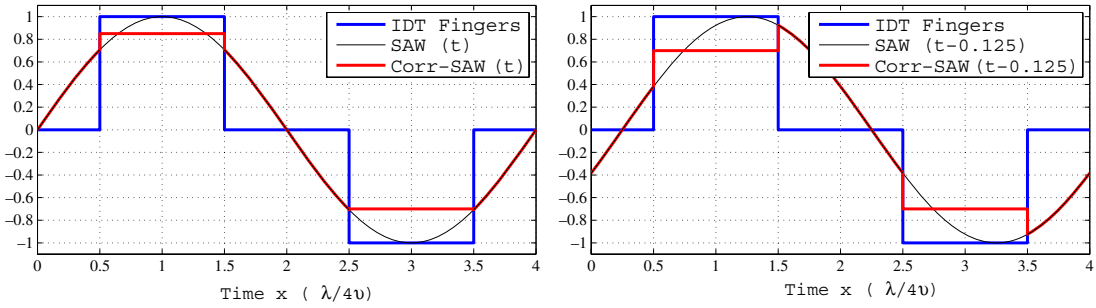

(a) time = t (b) time = t –T/8

Figure 7. Correlation between SAW electric potential and the output IDT of the SAW device. For a periodic IDT structure, one finger pair is represented, hence one time period ($T = \lambda/v$) is considered. Equipotential IDT fingers are represented by square waves. (a) The electric potential of the propagating SAW, SAW(t), is peaked at the centre of the output IDT fingers (considered at time t). (b) The electric potential of the propagating SAW is $T/8$ s delayed compared to SAW(t). In both cases, the cross-correlated electric signal consists of equipotentials across the IDT fingers.

conditions applicable for the SAW device based actuator model.

Mechanical boundary conditions

The IDT mass at the output IDT is taken to be negligible for simplicity, so that the mechanical force acting on the SAW substrate can be discarded. Hence the surface is considered to be mechanically free, and can be mathematically expressed as

$$\sum_j T_{3j} = 0, \tag{23}$$

where T is the mechanical stress tensor and $j = 1$–3.

Electrical boundary conditions

The conductive plate in the actuator model (figure 3) is placed at a height h above the output IDT, and connected to the common ground of the device. Therefore, the electric potential approaches zero at $x_3 = h$. The electric potential above the SAW substrate satisfies Laplace's equation, which results in an exponentially decaying electric signal in the x_3 direction, and can be written as

$$\Phi_L(x_1, x_3, t) = [A_L e^{kx_3} + B_L e^{-kx_3}]e^{ik(x_1 - vt)}, \tag{24}$$

for A_L and B_L constants. Furthermore, the electric potential and the electric flux density in the x_3 direction are continuous at the surface ($x_3 = 0$) [11, 24], which can be mathematically expressed as

$$\begin{aligned} \Phi(x_3 = 0^-) = \Phi(x_3 = 0) = \Phi(x_3 = 0^+), \\ D(x_3 = 0^-) = D(x_3 = 0) = D(x_3 = 0^+). \end{aligned} \tag{25}$$

Equations (22) and (25) are utilized to eliminate A_L and B_L in equation (24). Due to the conductive plate, the electric potential at $x_3 = h$ becomes zero. Therefore, from equation (24),

$$\begin{aligned} \Phi_L(x_1, h, t) = [A_L e^{kh} + B_L e^{-kh}]e^{ik(x_1 - vt)} = 0, \\ B_L = -A_L e^{2kh}. \end{aligned} \tag{26}$$

Once B_L is eliminated, equation (24) can be rewritten as

$$\Phi_L(x_1, x_3, t) = A_L[e^{kx_3} - e^{2kh - kx_3}]e^{ik(x_1 - vt)}. \tag{27}$$

The electrical boundary condition at the surface of the substrate ($x_3 = 0$) is considered to evaluate A_L. From the plane wave equation (22) for electric potential and equation (27), and the continuity equations (25), A_L can be evaluated as follows:

$$\begin{aligned} &\Phi_L(x_1, 0, t) = \Phi(x_1, 0, t), \\ &A_L[1 - e^{2kh}]e^{ik(x_1 - vt)} = \left[\sum_m C_m \alpha_4^m\right] e^{ik(x_1 - vt)}, \\ &\text{and} \qquad A_L = \frac{\sum_m C_m \alpha_4^m}{[1 - e^{2kh}]}. \end{aligned} \tag{28}$$

The relationship between the electric flux density and the electric field can be written as $D = \varepsilon_0 E$. Considering this relation along with equation (1), a relationship between the electric flux density and the electric potential in the gap in the x_3 direction can be written as

$$D_3(x_1, x_3, t) = -\varepsilon_0 \frac{\partial \Phi_L(x_1, x_3, t)}{\partial x_3}. \tag{29}$$

Hence, using the above equation, the electric flux density at $x_3 = 0$ is calculated and written as follows.

$$D_3(x_1, 0, t) = -k\varepsilon_0 \frac{\sum_m C_m \alpha_4^m [1 + e^{2kh}]}{[1 - e^{2kh}]} e^{ik(x_1 - vt)}. \tag{30}$$

Additionally, another alternative expression for the electric flux density at $x_3 = 0$ can be obtained from equation (6). Therefore,

$$D_3(x_1, 0, t) = \sum_j \sum_k e_{3jk} S_{jk} + \sum_j \varepsilon_{3j}^S E_j. \tag{31}$$

Ultimately, by equating equations (30) and (31), another eigenvalue problem is formulated, where the variables consist of the weighting coefficients. The resulting boundary conditions can be written out in matrix form as follows.

$$\begin{bmatrix} \mathbb{G} & 0 & \mathbb{H} & \mathbb{I} \\ \mathbb{J} & 0 & \mathbb{L} & \mathbb{N} \\ 0 & \mathbb{P} & 0 & 0 \\ \mathbb{Q} & 0 & \mathbb{R} & \mathbb{Y} \end{bmatrix} \begin{bmatrix} C_1 \\ C_2 \\ C_3 \\ C_4 \end{bmatrix} = 0, \tag{32}$$

where

$$\mathbb{G} = (c_{13} - c_{14}b^1)\alpha_1^1 + (-c_{14} + c_{11}b^1)\alpha_3^1 + (e_{13} - e_{22}b^1)\alpha_4^1$$
$$\mathbb{H} = (c_{13} - c_{14}b^3)\alpha_1^3 + (-c_{14} + c_{11}b^3)\alpha_3^3 + (e_{13} - e_{22}b^3)\alpha_4^3$$
$$\mathbb{I} = (c_{13} - c_{14}b^4)\alpha_1^4 + (-c_{14} + c_{11}b^4)\alpha_3^4 + (e_{13} - e_{22}b^4)\alpha_4^4$$
$$\mathbb{J} = c_{44}b^1\alpha_1^1 + (c_{44} - c_{14}b^1)\alpha_3^1 + e_{51}\alpha_4^1$$
$$\mathbb{L} = c_{44}b^3\alpha_1^3 + (c_{44} - c_{14}b^3)\alpha_3^3 + e_{51}\alpha_4^3$$
$$\mathbb{N} = c_{44}b^4\alpha_1^4 + (c_{44} - c_{14}b^4)\alpha_3^4 + e_{51}\alpha_4^4$$
$$\mathbb{P} = (c_{14} + c_{66}b^2)\alpha_2^2$$
$$\mathbb{Q} = e_{51}b^1\alpha_1^1 + (e_{51} + e_{22}b^1)\alpha_3^1 - (\varepsilon_{11}b^1 + \mathrm{i}\varepsilon_0\mathbb{X})\alpha_4^1$$
$$\mathbb{R} = e_{51}b^3\alpha_1^3 + (e_{51} + e_{22}b^3)\alpha_3^3 - (\varepsilon_{11}b^3 + \mathrm{i}\varepsilon_0\mathbb{X})\alpha_4^3$$
$$\mathbb{Y} = e_{51}b^4\alpha_1^4 + (e_{51} + e_{22}b^4)\alpha_3^4 - (\varepsilon_{11}b^4 + \mathrm{i}\varepsilon_0\mathbb{X})\alpha_4^4$$
$$\mathbb{X} = \frac{1 + \mathrm{e}^{2hk}}{1 - \mathrm{e}^{2hk}}.$$

Here the value of $\mathbb{X}$ depends on the position of the conductive plate above the SAW device (h), and takes the value of -1 for the case where the plate is at an infinite height above the substrate ($h \longrightarrow \infty$). In this analysis, the phase velocity is explicitly present in equations (16) and (17), and implicitly present in the roots b^m and in the linear coefficients α^m as mentioned before. Therefore, a suitable value for phase velocity should be chosen for which the determinant of the coefficients in the eigenvalue problem presented in equation (32) vanishes, hence satisfying the associated boundary conditions.

The above two eigenvalue problems presented in equations (15) and (32) are required to be solved simultaneously using iterative numerical procedures. This is due to the implicit dependence of decaying constants b^m on phase velocity v, and explicit dependence of eigenvectors of linear coefficients α^m on v. Once a suitable phase velocity is found, the weighting coefficients C_m can be determined. As a result, a complete solution is obtained for the electric potential at the output IDT (equation (22)).

7.1. Electrostatic coupling equations

In electrostatic actuation, the electrostatic force applied on two parallel plates can be described using the parallel plate capacitor effect [1] as

$$F = \frac{1}{2}\frac{\varepsilon A \Phi^2}{(h - W_\mathrm{P})^2}, \tag{33}$$

where ε is the dielectric coefficient of the medium between the plates, A is the effective plate area, $W_\mathrm{P}(x_1)$ is the instantaneous deflection of the actuator in the x_3 direction, h is the initial plate spacing, and Φ is the applied electric potential between the plates.

As is explained in section 4, an electrostatic force is generated between the output IDT and the conductive plate, due to the time varying electric potential at the output IDT. To formulate this force, each finger gap is divided into N_s subdivisions in the x_1 direction, so that each subdivision has a width of $\frac{f_\mathrm{w}}{N_\mathrm{s}}$ and a length of f_l (≈aperture of the IDT). Combining equations (22) and (33), and after some algebraic simplifications, the total resultant electrostatic force can be evaluated as

$$F_{(\mathrm{tot})} = \frac{C_t}{(h - W_\mathrm{P})^2}\sum_j \left[\left(\frac{2T}{\pi^2}\right)^2 \Phi^2\left(\frac{\lambda}{8}, x_3, t\right) + \Phi^2\left(\frac{\lambda}{4} + \frac{j\lambda}{4N_\mathrm{s}}, x_3, t\right)\right] \tag{34}$$

for $j = 1, 2, 3, \ldots, N_\mathrm{s}$ and $C_t = \frac{\varepsilon_0 f_l f_\mathrm{w} N_\mathrm{p}}{N_\mathrm{s}}$.

As the doubly clamped actuator is deflected due to the applied electrostatic force, an elastic restoring force is developed in the actuator. At equilibrium, the kinetic energy becomes zero, and the actuator's potential energy reaches a maximum. Therefore, to determine the displacement achieved by the actuator, the calculated electrostatic force and the elastic restoring force need to be considered at their equilibrium point [25, 26]. However, this becomes a complex problem to solve since both the forces depend on the actuator's instantaneous displacement $W_\mathrm{p}(x_1)$. Therefore, to obtain an accurate solution for $W_\mathrm{P}(x_1)$, analytical methods or numerical analysis methods such as FEM are required.

8. The Rayleigh–Ritz method

In order to prove the feasibility of the suggested design, and compare with the FEA results to validate the design, a reduced order model of the actuator is first built using the Rayleigh–Ritz method. Following the minimum potential energy analysis for a beam presented by Washizu [25], the total potential energy of the actuator, modelled in the framework of the Euler–Bernoulli theory, can be deduced. For a doubly clamped actuator with a length of l, the total energy E_act of the actuator under a pressure P can be written as

$$E_\mathrm{act} = \frac{1}{2}\int_0^l \mathbb{E}I\left(\frac{\partial^2 W_\mathrm{p}}{\partial {x_1}^2}\right)^2 - \int_0^l P W_\mathrm{p}\,\mathrm{d}x_1, \tag{35}$$

where $\mathbb{E}$ is the modulus of elasticity, $W_\mathrm{P}(x_1)$ is the lateral displacement (in the x_3 direction), and I is the moment of inertia of the cross-section. Considering the relation $F = PA$, where A is the effective actuator area, the second integral component in equation (35) can be rearranged using the electrostatic force, which is derived in equation (34). Additionally, the displacement function $W_\mathrm{p}(x_1)$ must satisfy the essential homogeneous boundary conditions of the actuator, which is presented as follows.

$$W_\mathrm{p}(0) = W_\mathrm{p}(l) = 0,$$
$$\left.\frac{\partial W_\mathrm{p}}{\partial t}\right|_{x_1=0} = \left.\frac{\partial W_\mathrm{p}}{\partial t}\right|_{x_1=l} = 0. \tag{36}$$

Even though there exist various base functions that satisfy the essential boundary conditions of the model, care was taken to select a function with a better representation of the actuator model [27]. Here, a base function for the actuator is selected as in equation (37), with the only unknown being the coefficient K_P.

$$W_\mathrm{P}(x_1) = K_\mathrm{P} x_1^2 (l - x_1)^2. \tag{37}$$

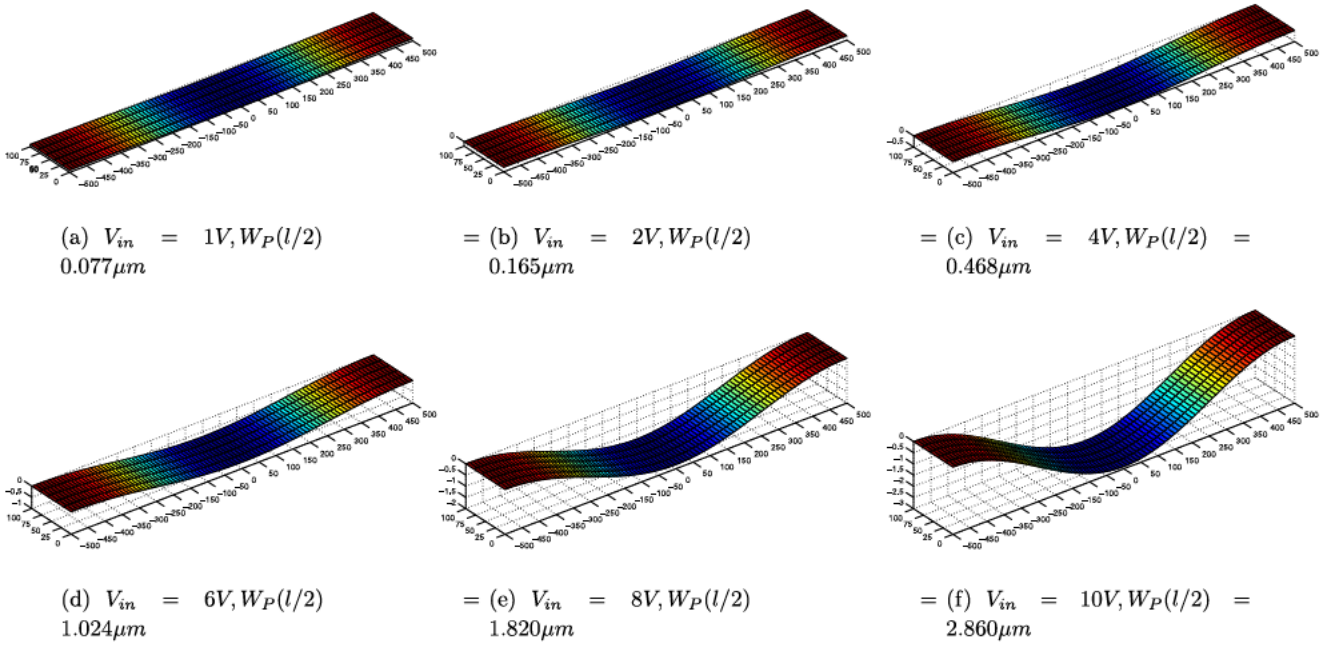

(a) $V_{in} = 1V, W_P(l/2) = 0.077\mu m$ (b) $V_{in} = 2V, W_P(l/2) = 0.165\mu m$ (c) $V_{in} = 4V, W_P(l/2) = 0.468\mu m$

(d) $V_{in} = 6V, W_P(l/2) = 1.024\mu m$ (e) $V_{in} = 8V, W_P(l/2) = 1.820\mu m$ (f) $V_{in} = 10V, W_P(l/2) = 2.860\mu m$

Figure 8. Mid-beam deflection ($W_P(l/2)$) of the actuator for different input voltages (V_{in}). As the control voltage increases, $W_P(l/2)$ increases at an increasing rate. The dimensions of the analysed actuator are 1000 μm × 100 μm (length × width).

As can be seen, the function in equation (37) satisfies the essential boundary conditions expressed in equation (36). According to the Rayleigh–Ritz method, the equilibrium of the plate can be found by minimizing the total energy E_{act} with respect to K_P. In achieving this, first total energy can be expressed in terms of K_P by substituting equations (34) and (37) into equation (35). Then the equilibrium is found from the condition

$$\frac{\partial E_{act}}{\partial K_P} = 0. \tag{38}$$

An iterative approach is needed until the convergence is achieved due to the complicated nonlinear coupling between equations (34), (35) and (37). Actuator deformations for various operating voltages are achieved and presented in figure 8. Here, it is evident that as the control signal amplitude increases the static mid-beam displacement of the actuator increases. The results based on this analytical modelling, especially the relationship between the beam deflection and the input voltage, are further considered in section 10.1, in validating the FEM of the proposed SAW based actuator model.

In general, analytical approaches with lesser simplifications are quite complicated and require extensive computational effort. It is known that more accurate results for such problems can be achieved through numerical analysis using mathematical methods such as finite element analysis (FEA) [27, 28]. Because of the complexity in analysis, which involves electrostatic and structural field coupling, FEA of the microactuator is developed using ANSYS simulation tools and presented in section 9.

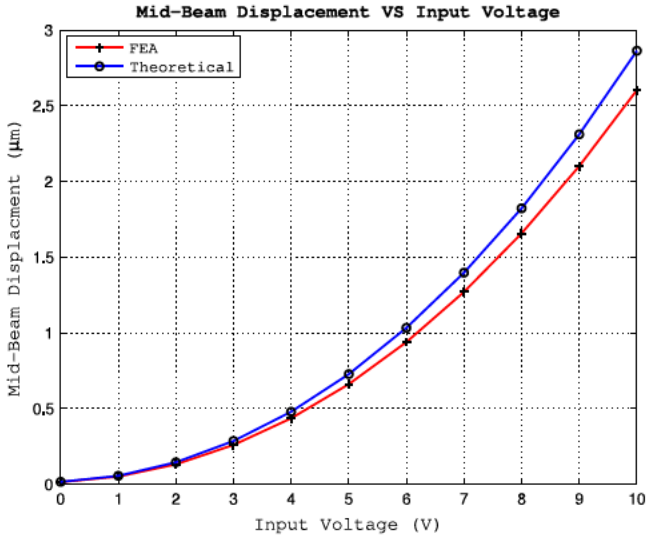

Figure 9. Comparison of simulated and theoretical results for the SAW actuator. Displacement versus voltage plot for the mid-beam displacement of the actuator.

9. Finite element modelling of the actuator

A coupled-field analysis is required to model the electrostatic–solid interaction of the microactuator. Generally, direct coupling is advantageous for coupled-field interactions, which involve strongly coupled physics, or high nonlinearity, which is best solved in a single solution. However, analyses based on load transfer methods are more efficient and flexible because the different field analyses could be performed independently. A load transfer method based ANSYS multi-field solver (MFX) is available for a large class of coupled analysis problems, and more suitable for MEMS based coupled-field analysis, which involves interaction between multiple physical fields [28]. Therefore, in this research, the ANSYS-MFX solver is used to analyse the microactuator performance.

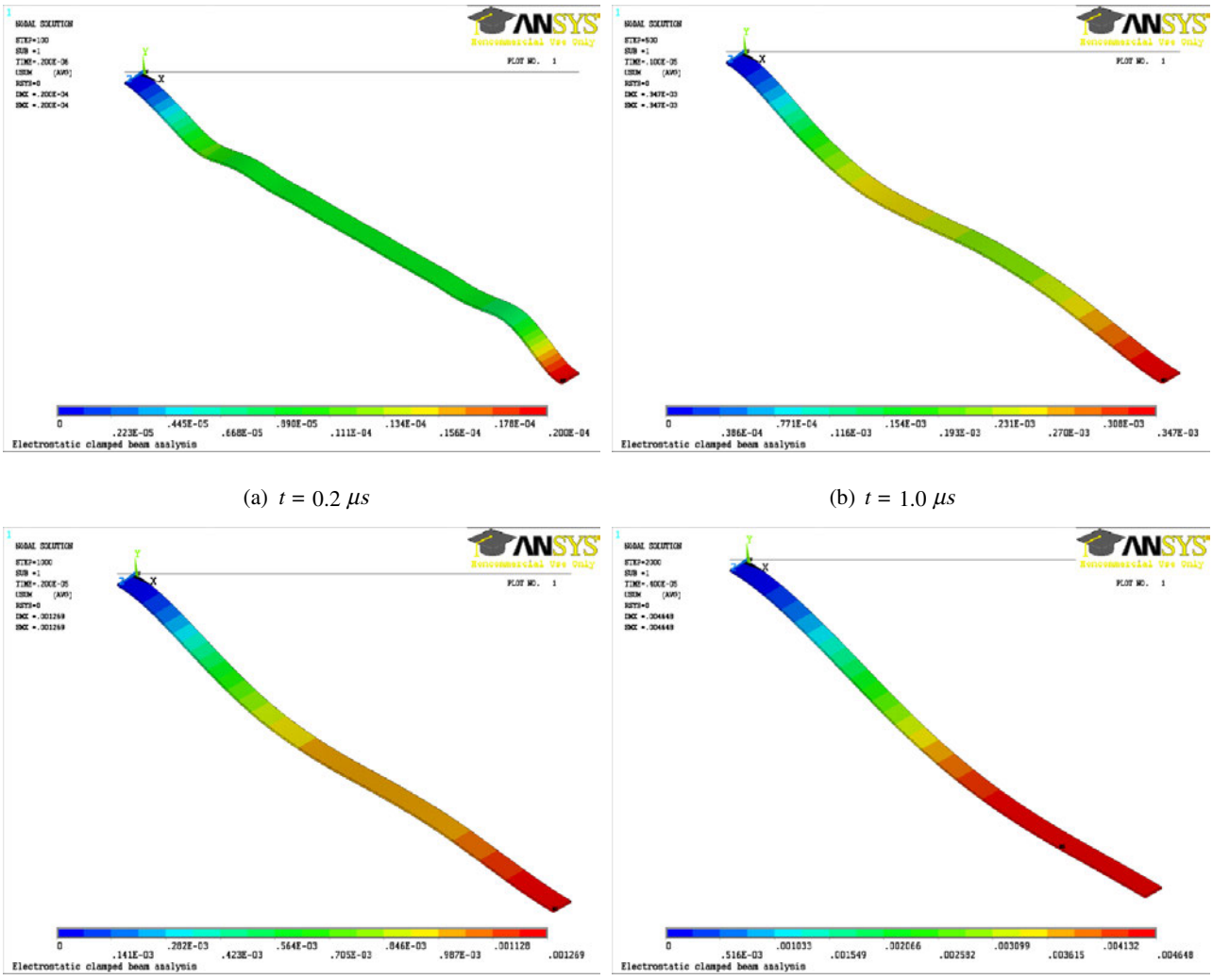

(a) $t = 0.2\ \mu s$ (b) $t = 1.0\ \mu s$

(c) $t = 2.0\ \mu s$ (d) $t = 4.0\ \mu s$

Figure 10. Deflection results for the actuator at various time steps during the transient analysis. Half-symmetry is exploited due to the symmetrical nature of the model. The flexural behaviour is observed during the stabilization period.

The SOLID95 3D element type is used for the structural model, and the electrostatic air gap is meshed using the SOLID122 element type. To simplify the analysis and to improve the simulation time and efficient CPU usage, the performance of a thin conductive plate with a smaller width was initially considered, and half-symmetry is exploited due to the symmetrical nature of the model.

10. FEA simulations and results

10.1. Static analysis

During the analysis, to mimic the effect of the electric potential wave generated at the output IDT, a set of interleaved electrodes was used and every other electrode was coupled, so that one set of electrodes acts as the positive bus bar and the other as the negative bus bar. Material properties of silicon were used for the doubly clamped conductive plate. The plate dimensions were 1000 μm $\times$ 2 μm $\times$ 10 μm ($L \times H \times W$). The air gap between the electrodes and the conductive plate h was 10 μm. For static analysis, a 10 V input voltage was applied to the positive bus bar. The negative bus bar and the conductive plate were connected to a common ground.

Initial FEA results are verified using the Rayleigh–Ritz method based analytical model. Displacement versus voltage results were plotted and are shown in figure 9. A good correlation can be observed between the analytical and simulation results for the microactuator. However, FEA results demonstrate slightly lower displacements for a given voltage. This is mainly because the full thickness of the actuator was considered in the simulated 3D model in FEA, whereas the actuator was modelled as a thin plate in the Rayleigh–Ritz method based analytical model. Therefore, the higher bending stiffness reduces the effective mid-beam displacement in the FEA model. It should be noted that the actuator displacement can be increased by reducing the gap between the conductive plate and the output IDT, reducing the thickness of the conductive plate, and reducing the stress level applied at the actuator by optimizing the clamping mechanism.

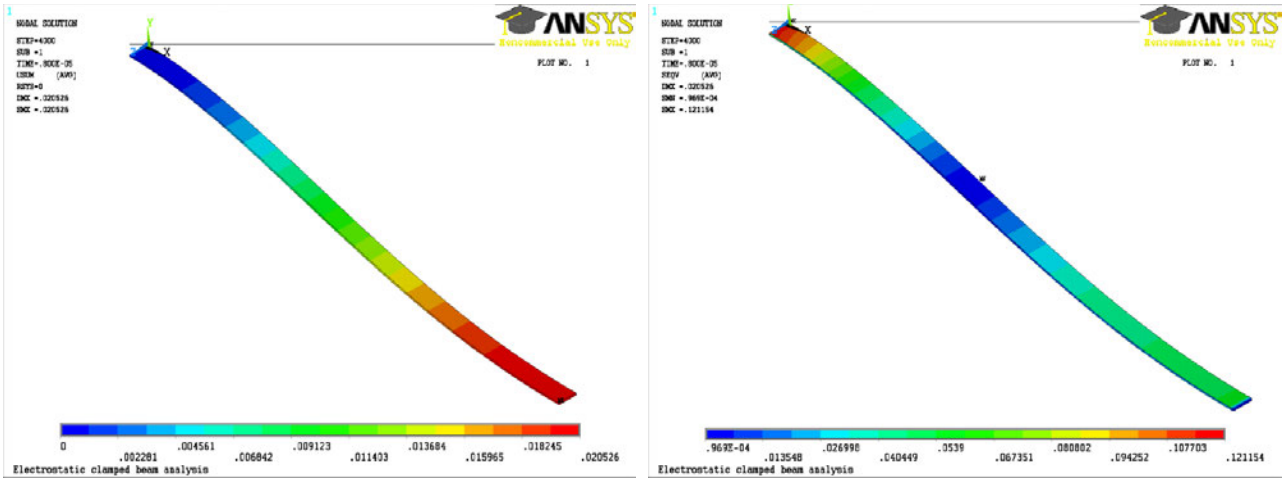

(a) Displacement. (b) Von Mises stress.

Figure 11. Deflection and Von Mises stress analysis results for the actuator performance at $t = 8.0\ \mu$s (final step). The maximum Von Mises stress in this scenario is 0.121 MPa, which is near the clamped edge.

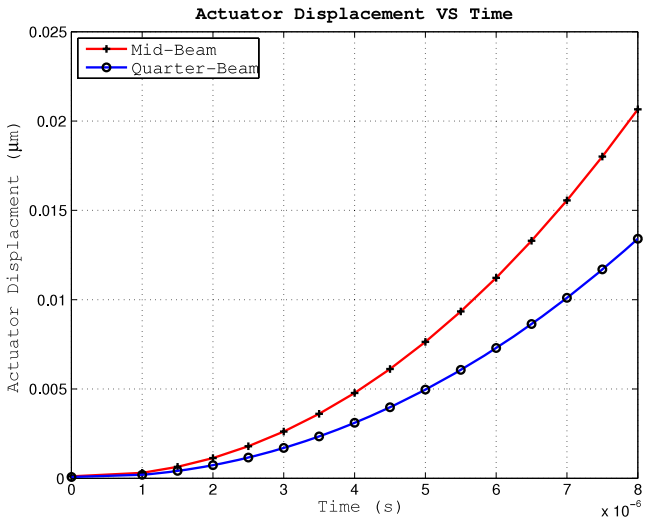

Figure 12. Displacement versus time plot of the mid-beam. Analysis carried out for 400 T, where T is the time period of the SAW signal.

10.2. Transient analysis

For transient analysis of the actuator, an AC sinusoidal wave with a frequency of 50 MHz and a peak voltage of 10 V were used to emulate the electric potential wave at the output IDT as proven in equation (22). However, due to the constraints introduced by factors such as node density and the CPU processing power, transient simulations were performed for a time range of 400 T during this analysis, where T is the time period of the SAW.

Figures 10 and 11 depict transient analysis results. As a thinner actuator is modelled in ANSYS, the flexural behaviour of the actuator is first observed. As the time progresses, the deflection profile of the actuator is found to be similar to the profile obtained from the Rayleigh–Ritz method based analysis.

Figure 11(b) depicts the contour plot of the Von Mises stress distribution of the actuator. Here, the Von Mises stress can be used to predict the yielding of any of the materials used, under any loading condition. The maximum Von Mises stress in this scenario is 0.121 MPa, which is much lower than the yield strengths of the selected material. This demonstrates that the actuator's deflection is well within the elastic range of the materials used.

Microdisplacements are successfully obtained using the SAW actuator. Figure 12 shows the mid-beam and the quarter-beam displacement variations over a simulation time of 400 T. Based on the static analysis, however, it was shown that displacements up to $\sim$3 μm can be achieved from this model. As a result, it is proven that, even after 400 T, still the dynamic displacement does not show any periodic nature but is in the process of gaining more displacement. This demonstrates that the actual operating frequency of the actuator is a very much scaled down version of the SAW frequency.

11. Conclusion

A novel, wirelessly and securely interrogated, batteryless and passive microactuator for bio-MEMS is discussed and demonstrated in this paper. In designing the model, the requirements imposed by the current and emerging biomedical applications on these devices such as small size, passivity, bio-compatibility, and remote interrogability are taken into consideration. As a result the proposed device can be used in the design of microvalves and micropumps for biomedical applications such as drug delivery, DNA sequencing, and flow cytometry, where the performance of the microactuator is critical.

Theoretical analysis of the entire SAW based actuator operation was carried out and boundary conditions applicable for the presented design were used to derive the electric potential wave forms, and hence the electrostatic field between the SAW device and the actuator. The significance in the

use of FEA to simulate and analyse complex scenarios, as an alternative option to analytical modelling, is highlighted. Then, detailed FEM was carried out and static analysis results were generated using the ANSYS simulation tool, and compared with the theoretical results obtained by Rayleigh–Ritz method. A good correlation between the theoretical and simulated displacement curves were observed.

Consequently, the dynamic behaviour of the SAW based actuator was investigated using transient analysis. This is more substantial in investigating the operating frequency of the conductive plate. Since the SAW frequency is in the range between 50 MHz and 1 GHz, it was crucial to verify the effective operating frequency of the conductive plate. Because of the time varying electrostatic field, it was found that the oscillating frequency of the actuator is much less than the SAW frequency, which is much desired for better control.

As potential future work, in addition to integrated device fabrication, as a useful extension to current work, the multiple code coupling method in the ANSYS-MFX solver combined with ANSYS-CFX could be used to develop an implantable micropump and simulate a complete electrostatic–structure–fluid interaction problem, to optimize the design parameters of such a device. This will allow a complete simulation model that could be used to analyse similar microfluidic devices at design stage, before fabrication.

Acknowledgments

The authors would like to thank the Australian Research Council (ARC) and the School of Electrical and Electronic Engineering, The University of Adelaide, Australia, for providing the necessary funding, facilities, and support to carry out this research.

References

[1] Tsai N C and Sue C Y 2007 Review of MEMS-based drug delivery and dosing systems *Sensors Actuators* A **134** 555–64

[2] Varadan V K and Varadan V V 2000 Microsensors, micromechanical systems (MEMS), and electronics for smart structures and systems *Smart Mater. Struct.* **9** 953–72

[3] Jones I *et al* 2008 Wireless RF communication in biomedical applications *Smart Mater. Struct.* **17** 015050

[4] Pitz I, Hall L T, Hansen H J, Varadan V K, Bertram C D, Maddocks S, Enderling S, Saint D, Al-Sarawi S F and Abbott D 2002 Trade-offs for wireless transcutaneous RF communication in biotelemetric applications *Proc. SPIE—Biomed. Appl. Micro Nanoeng.* **4937** 307–18

[5] Medtronic Incorporation 2010 Medtronic home page http://www.medtronic.com/ accessed 27/10/2010

[6] Prescott J H, Lipka S, Baldwin S, Sheppard J, Maloney J M, Coppeta J, Yomtov B, Staples M A and Santini J 2006 Chronic, programmed polypeptide delivery from an implanted, multireservoir microchip device *Nat. Biotechnol.* **24** 437–8

[7] Wixforth A 2003 Acoustically driven planar microfluidics *Superlatt. Microstruct.* **6** 389–96

[8] Strobl C J, Guttenberg Z V and Wixforth A 2004 A nano-and pico-dispensing of fluids on planar substrates using SAW *IEEE Trans. Ultrason. Ferroelectr. Freq. Control* **51** 1432–6

[9] Dissanayake D W, Tikka A C, Al-Sarawi S and Abbott D 2007 Radio frequency controlled microvalve for biomedical applications *Proc. SPIE—Smart Mater. IV* **6413** 64130D

[10] Ruppel C C W, Reindl L and Weigel R 2002 SAW devices and their wireless communication applications *IEEE Microw. Mag.* **3** 65–71

[11] Subramanian H, Varadan V K, Varadan V V and Vellekoopz M J 1997 Design and fabrication of wireless remotely readable MEMS based microaccelerometers *Smart Mater. Struct.* **6** 730–8

[12] Dissanayake D W, Al-Sarawi S, Lu T and Abbott D 2009 Finite element modelling of SAW device based corrugated micro-diaphragms *Smart Mater. Struct.* **18** 095030

[13] Tikka A C, Al-Sarawi S and Abbott D 2008 A remotely interrogatable passive microactuator using SAW correlation *3rd Int. Conf. on Sensing Technology* pp 46–51

[14] Schmidt F, Sczesny O, Ruppel C and Magori V 1996 Wireless interrogator system for SAW-identification-marks and SAW-sensor components *Proc. 50th IEEE Int. Symp. on Frequency Control* pp 208–15

[15] Zaglmayr S, Schöberl J and Langer U 2005 *Mathematics in Industry* vol 8 *Progress in Industrial Mathematics at ECMI 2004* (Berlin: Springer) chapter (Eigenvalue Problems in Surface Acoustic Wave Filter Simulations) pp 75–99

[16] Gantner A, Hoppe R H W, Köster D, Siebert K G and Wixforth A 2007 Numerical simulation of piezoelectrically agitated surface acoustic waves on microfluidic biochips *Comput. Vis. Sci.* **10** 145–61

[17] Adler E L 2000 Bulk and surface acoustic waves in anisotropic solids *Int. J. High Speed Electron. Syst.* **10** 653–84

[18] Kannan T 2006 Finite element analysis of surface acoustic wave resonators *Master's Thesis* University of Saskatchewan

[19] Wolfram MathWorld 2010 Euler angles http://mathworld.wolfram.com/EulerAngles.html accessed 25/05/2010

[20] Upadhyay S K 2004 *Seismic Reflection Processing: With Special Reference to Anisotropy* 1st edn (Berlin: Springer) chapter (Anisotropy Models of Sedimentary Sections and Characteristics of Wave Propagation) pp 143–201

[21] Gardner J W, Varadan V K and Awadelkarim O O 2001 *Microsensors, MEMS, and Smart Devices* 1st edn (Beijing: Tsinghua University Press) chapter (Microsensors, Introduction to SAW Devices, Surface Acoustic Waves in Solids, IDT Microsensor Parameter Measurement, IDT Microsensor Fabrication, IDT Microsensors) pp 227–396

[22] Ippolito S J, Kalantar-zadeh K, Wlodarski W and Powell D A 2002 Finite-element analysis for simulation of layered SAW devices with XY LiNbO3 substrate *Proc. SPIE—Smart Struct. Devices Syst.* **4935** 120–31

[23] Skinner J L, Cardinale G F, Talin A A and Brocato R W 2006 Effect of critical dimension variation on SAW correlator energy *IEEE Trans. Ultrason. Ferroelectr. Freq. Control* **53** 497–501

[24] Maugin G A 1985 *Nonlinear Electromachanical Effects and Applications* 1st edn (Singapore: World Scientific) chapter (Rayleigh Surface Waves) pp 104–42

[25] Washizu K 1975 *Variational Methods in Elasticity and Plasticity* 2nd edn (Oxford: Pergamon) chapter (Beams, Plates) pp 132–82

[26] Hu Y C, Chang C M and Huang S C 2004 Some design considerations on the electrostatically actuated microstructures *Sensors Actuators* A **112** 155–61

[27] Bao M H 2000 Basic mechanics of beams and diaphragm structures *Micro Mechanical Transducers: Pressure Sensors, Accelerometers, and Gyroscopes (Hand Book of Sensors and Actators)* vol 8 (New York: Elsevier) pp 23–87

[28] Nisar A, Afzulpurkar N, Mahaisavariya B and Tuantranont A 2008 Multifield analysis using multiple code coupling of a MEMS based micropump with biocompatible membrane materials for biomedical applications *Proc. Int. Conf. on BioMedical Engineering and Informatics* vol 1, pp 531–5